View metadata, citation and similar papers at core.ac.uk

brought to you by CORE

provided by NASA Technical Reports Server

NASA/CR- -1998- 207465

AIAA 98-0183

Perfectly Matched Layer for Linearized Euler Equations in Open and Ducted Domains

C. K. W. Tam and L. Auriault
Florida State University
Tallahassee, FL

F. Cambuli
Universita degli Studi di Cagliari
Cagliari, Italy

36th Aerospace Sciences Meeting & Exhibit
January 12–15, 1998 / Reno, NV

For permission to copy or republish, contact the American Institute of Aeronautics and Astronautics
1801 Alexander Bell Drive, Suite 500, Reston, Virginia 20191-4344

Perfectly Matched Layer as Absorbing Boundary Condition for the Linearized Euler Equations in Open and Ducted Domains[†]

Christopher K.W. Tam* and Laurent Auriault**
Department of Mathematics
Florida State University
Tallahassee, FL 32306-4510
tam@math.fsu.edu

Francesco Cambuli***
Dipartimento di Ingegneria Meccanica
Universita degli Studi di Cagliari
Piazza d'Armi
09123 Cagliari, Italy

Abstract

Recently, perfectly matched layer (PML) as an absorbing boundary condition has found widespread applications. The idea was first introduced by Berenger for electromagnetic waves computations. In this paper, it is shown that the PML equations for the linearized Euler equations support unstable solutions when the mean flow has a component normal to the layer. To suppress such unstable solutions so as to render the PML concept useful for this class of problems, it is proposed that artificial selective damping terms be added to the discretized PML equations. It is demonstrated that with a proper choice of artificial mesh Reynolds number, the PML equations can be made stable. Numerical examples are provided to illustrate that the stabilized PML performs well as an absorbing boundary condition. In a ducted environment, the wave mode are dispersive. It will be shown that the group velocity and phase velocity of these modes can have opposite signs. This results in a band of transmitted waves in the PML to be spatially amplifying instead of evanescent. Thus in a confined environment, PML may not be suitable as an absorbing boundary condition.

1. Introduction

Recently, Berenger[1,2] succeeded in formulating an absorbing boundary condition for computational electromagnetics that has the unusual characteristic that when an outgoing disturbance impinges on the interface between the computation domain and the absorbing layer surrounding it, no wave is reflected back into the computation domain. In other words, all the outgoing disturbances are transmitted into the absorbing layer where they are damped out. Such a layer has come to be known as a perfectly matched layer (PML).

Since its initial development, PML has found widespread applications in elastic wave propagation[3], computational aeroacoustics and many other areas. Hu[4] was the first to apply PML to aeroacoustics problems governed by the linearized Euler equations; linearized over a uniform mean flow. He has since extended his work to nonuniform mean flow and for the fully nonlinear Euler equations[5]. Further applications of PML to acoustics problems including wavemodes in ducts can be found in the most recent works of Hu and coworkers[6,7]. In these references, examples are provided that indicate that high quality numerical solutions could be found with PML used as radiation or outflow boundary conditions.

In open unbounded domains, acoustic waves are nondispersive and propagate with the speed of sound relative to the local mean flow. Inside a duct, the situation is completely different. Acoustic waves are repeatedly reflected back by the confining walls. For ducts with parallel walls, the continuous reflection of the acoustic waves by the wall leads to the formation of coherent wave patterns called duct modes[8,9]. Unlike the open domain, duct modes are dispersive with phase and group velocities vary with axial wavenumber. Because of the dispersive nature of the duct modes many radiation boundary conditions that work well in open domains are known to be inappropriate for ducted environments. For this reason, Tam[10] in a recent review on numerical

† Copyright ©1998 by C.K.W. Tam. Published by the American Institute of Aeronautics and Astronautics, Inc. with permission.

* Distinguished Research Professor, Department of Mathematics. Associate Fellow AIAA

** Graduate Student, Department of Mathematics.

*** Visiting Scholar, Department of Mathematics, Florida State University.

boundary conditions for computational aeroacoustics, suggested that boundary condition for ducted environment be regarded as a category of its own.

There are three primary objectives in this work. First, we intend to show that in the presence of a mean flow normal to a PML, the standard PML equations of the linearized Euler equations support unstable solutions. Earlier Tam[10] had pointed out that the PML equations with mean flow have unstable solutions. However, he did not show that the existence of instabilities is due to the mean flow component normal to the layer. The origin and characteristics of these instabilities are investigated and analyzed. It is interesting to mention that in his earliest work, Hu[4] reported that his computation encountered numerical instability. But by applying numerical filtering, he was able to obtain stable solutions. In light of our finding, we believe that what Hu encountered was not instability of his numerical scheme but that his numerical solution inadvertently excited the intrinsic unstable solution of the PML equations. Not directly related to the instability of the PML equations, Abarbanel and Gottlieb[11] recently analyzed the electromagnetic PML equations. They concluded that the equations are only weakly well-posed.

Second, we will show that the instability is not very strong, namely, the growth rates are small. Also the instabilities are confined primarily to short waves. It is, therefore, possible to suppress the instabilities by the addition of artificial selective damping terms[12] to the discretized PML equations. It is important to point out that artificial selective damping eliminates mainly the short waves and has negligible effect on the long or the physical waves. Thus the addition of these damping terms does not effect the perfectly matched conditions of the PML.

Third, we will show that a perfectly matched layer may not be suitable as an absorbing boundary condition for waves in a ducted flow environment. The major difference between acoustic waves in an open domain and acoustic waves inside a duct is that in an unbounded region acoustic waves are nondispersive whereas duct modes are dispersive. It will be shown that in the presence of a mean flow the group and phase velocity of the duct modes can have opposite signs. Because of this, a band of transmitted waves will actually grow spatially instead of being damped in the PML. In other words, the PML equations do not damp these wave modes as absorbing boundary condition ought to do. The exception is when there is no mean flow in the duct. In this special case, all the transmitted waves are spatially damped.

In section 2, the use of PML for open domain problems is discussed. The stability of the PML governing equations are investigated. It will be shown that the addition of damping terms to form the PML equations can actually cause the vorticity and acoustic wave modes to become unstable. The splitting of the variables in formulating the PML equations leads to a higher order system of equations. This higher system supports extra solutions. These extra or spurious solutions are found to become unstable when the damping coefficient is large. Numerical examples are provided to illustrate the spread of the unstable solution from the PML back into the interior of the computation domain.

In section 3, the effect of the addition of artificial selective damping terms to the discretized PML equations is investigated. It is shown that with an appropriate choice of mesh Reynolds number, the unstable solutions of the PML equations can be suppressed. Numerical examples are given to demonstrate the effectiveness of the modified PML as a radiation/outflow boundary condition.

Section 4 deals with the theory and application of PML to ducted internal flow problems. An eigenvalue analysis is carried out to show the existence of a band of frequency for which the PML exerts no damping on the acoustic duct modes. These wave modes actually would grow in amplitude as they propagate through the PML. Numerical results are provided to illustrate the existence of this kind of amplifying ducted acoustic modes.

2. Open Domain Problems

Let us consider the use of PML as absorbing boundary condition for the solution of the linearized Euler equations (linearized over a uniform mean flow) in a two-dimensional open domain as shown in figure 1. We will use $\Delta x = \Delta y$ (the mesh size) as the length scale, a_0 (the sound speed) as the velocity scale, $\frac{\Delta x}{a_0}$ as the time scale, $\rho_0 a_0^2$ (where ρ_0 is the mean density) as the pressure scale. The dimensionless governing equations in the PML are formed by splitting the linearized Euler equations according to the spatial derivatives. An absorption term is added to each of the equations with spatial derivative in the direction normal to the layer. For example, for the PML on the right boundary of figure 1, the governing equations are[4],

$$\frac{\partial u_1}{\partial t} + \sigma u_1 + M_x \frac{\partial}{\partial x}(u_1 + u_2)$$

$$+ \frac{\partial}{\partial x}(p_1 + p_2) = 0$$

$$\frac{\partial u_2}{\partial t} + M_y \frac{\partial}{\partial y}(u_1 + u_2) = 0$$

$$\frac{\partial v_1}{\partial t} + \sigma v_1 + M_x \frac{\partial}{\partial x}(v_1 + v_2) = 0$$

$$\frac{\partial v_2}{\partial t} + M_y \frac{\partial}{\partial y}(v_1 + v_2) + \frac{\partial}{\partial y}(p_1 + p_2) = 0$$

$$\frac{\partial p_1}{\partial t} + \sigma p_1 + M_x \frac{\partial}{\partial x}(p_1 + p_2) + \frac{\partial}{\partial x}(u_1 + u_2) = 0 \qquad (1)$$

$$\frac{\partial p_2}{\partial t} + M_y \frac{\partial}{\partial y}(p_1 + p_2) + \frac{\partial}{\partial y}(v_1 + v_2) = 0$$

where M_x and M_y are the mean flow Mach numbers in the x and y directions. σ is the absorption coefficient.

Suppose we look for solutions with (x, y, t) dependence in the form $\exp[i(\alpha x + \beta y - \omega t)]$. It is easy to find from (1) that the dispersion relations of the PML equations are,

$$\left(1 - \frac{\alpha M_x}{\omega + i\sigma} - \frac{\beta M_y}{\omega}\right)^2 - \frac{\alpha^2}{(\omega + i\sigma)^2} - \frac{\beta^2}{\omega^2} = 0 \quad (2)$$

$$1 - \frac{\alpha M_x}{\omega + i\sigma} - \frac{\beta M_y}{\omega} = 0. \qquad (3)$$

In the limit $\sigma \to 0$, (2) and (3) become the well-known dispersion relations of the acoustic and the vorticity waves of the linearized Euler equations.

2.1. Mean Flow Parallel to PML

Dispersion relations (2) and (3) behave very differently depending on whether there is any mean flow normal to the PML. When the mean flow is parallel to the layer; i.e., $M_x = 0$, the solutions are stable. This is easy to see from (3) for the vorticity wave. Physically, if the mean flow is parallel to the PML, the vorticity waves in the computation domain, being convected by the mean flow, cannot enter the layer and hence would not lead to unstable solution.

To show that for $M_x = 0$ all the solutions of (2) are stable, a simple mapping will suffice. Rewrite (2) in the form

$$F \equiv (\omega - \beta M_y)^2 - \frac{\alpha^2 \omega^2}{(\omega + i\sigma)^2} = \beta^2. \qquad (4)$$

Figure (2) shows the image of the upper-half ω-plane in the F plane. The upper-half ω-plane is mapped into the entire F plane except for the slit ADC. But since β^2 is real and positive, for subsonic mean flow the point β^2 lies outside the image. Thus no value of ω in the upper-half ω-plane would satisfy equation (2) indicating that there is no unstable solution.

2.2. Unstable Solutions of the PML Equations

For $M_x \neq 0$, the PML equations support unstable solutions. It is to be noted that, unlike the original dispersion relation of the acoustic waves, equation (2) is a quadric equation in ω. It has two extra roots in addition to the two modified acoustic modes. For small σ, the two spurious roots are damped but one of the modified acoustic roots is unstable. For larger σ, numerical solutions indicate that one of the spurious roots becomes unstable. In any case, the equation splitting procedure and the addition of an absorption term, both are vital to the suppression of reflections at the interface between the computation domain and the PML, inadvertently, lead to instabilities.

For small σ, the roots of (2) and (3) can be found by perturbation. Let,

$$\omega^{(a)} = \omega_0^{(a)} + \sigma\omega_1^{(a)} + \sigma^2\omega_2^{(a)} + \ldots \qquad (5)$$

$$\omega^{(v)} = \omega_0^{(v)} + \sigma\omega_1^{(v)} + \sigma^2\omega_2^{(v)} + \ldots \qquad (6)$$

where the roots of (2) and (3) are designated by a superscript 'a' (for acoustic waves) and 'v' (for vorticity waves). Substitution of (5) and (6) into (2) and (3), it is straightforward to find,

$$\omega_0^{(a)} = \omega_+, \quad \omega_-, \quad 0, \quad 0 \qquad (7)$$

where

$$\omega_\pm = (\alpha M_x + \beta M_y) \pm (\alpha^2 + \beta^2)^{\frac{1}{2}} \qquad (8)$$

$$\omega_1^{(a)} = i\left[\frac{-\alpha^2 \mp \alpha M_x(\alpha^2 + \beta^2)^{\frac{1}{2}}}{\alpha^2 + \beta^2 \pm (\alpha M_x + \beta M_y)(\alpha^2 + \beta^2)^{\frac{1}{2}}}\right] \qquad (9)$$

$$\omega_0^{(v)} = \alpha M_x + \beta M_y, \quad 0 \qquad (9)$$

$$\omega_1^{(v)} = \frac{-i}{1 + (\frac{M_y}{M_x})(\frac{\beta}{\alpha})}. \qquad (11)$$

Clearly if $\omega_1^{(a)}$ or $\omega_1^{(v)}$ has a positive imaginary part, the mode is unstable. It is easy to show, especially in the case $M_y = 0$, that there are always values of α and β such that $\omega_1^{(a)}$ of (10) is purely imaginary

and positive. Similarly, from (11) for $\frac{\beta}{\alpha} < 0$ and $|\frac{\beta}{\alpha}| > \frac{M_x}{M_y}$, $\omega_1^{(v)}$ is also purely positive imaginary. Thus the PML equations in the presence of a uniform flow with $M_x \neq 0$ support unstable solutions.

The unstable solutions of dispersion relations (2) and (3) can also be found numerically. For a given (α, β) the growth rates, ω_i, of the unstable solutions can be calculated in a straightforward manner. Figure (3) shows the ω_i contours of the most unstable solution of equation (2), the acoustic mode, in the $\alpha - \beta$-plane for the case $M_x = 0.3$, $M_y = 0.0$ and $\sigma = 1.5$. Figure 4 shows a similar plot for the vorticity wave mode (equation (3)). In these figures only the unstable regions are shown. It is clear that there are instability waves over a wide range of wavenumbers. Numerical results indicate that, in general, the unstable regions expand as the flow Mach number or the damping coefficient σ increases.

2.3. Numerical Examples

The nature and characteristics of the unstable waves associated with the acoustic mode and the vorticity mode are quite different. To illustrate the excitation of these unstable solutions in the PML by disturbances propagating or convecting from the interior computation domain, a series of numerical experiments has been carried out. Figure 5 shows the results of the case of a vorticity pulse convected into the PML when $M_x = 0.3$, $M_y = 0.2$ and $\sigma = 1.0$. The initial conditions for the pulse are (same as the initial conditions used by Tam & Webb[13])

$$
\begin{aligned}
&p = \rho = 0 \\
&u = 0.04y \exp\left[-(\ell n\, 2)\left(\frac{x^2+y^2}{25}\right)\right] \\
&v = -0.04x \exp\left[-(\ell n\, 2)\left(\frac{x^2+y^2}{25}\right)\right].
\end{aligned}
\tag{10}
$$

The DRP time marching scheme[13] is used in the simulation. The PML region extends from $x = 20$ to the right boundary of the computation domain. At the outermost boundary, the boundary condition $p_1 = p_2 = \rho_1 = \rho_2 = u_1 = u_2 = v_1 = v_2 = 0$ are imposed. Plotted in figure 5 are contours of the u velocity component. Figure 5a shows the initial profile of the contours at $t = 0$. Figure 5b, at $t = 50$, reveals that there is damping of the vorticity pulse as it begins to enter the PML. This damping is the result of the built-in damping, σ, of the PML. Figure 5c, at a later time $t = 90$, shows the growth of the excited unstable solution in the PML. Finally, figure 5d (at $t = 130$) shows the spread of the unstable solution back into the interior computation domain. Figure 6 gives the corresponding waveform of the vorticity wave pulse. Figure 6d clearly indicates that the spread of the unstable vorticity waves in the PML can quickly contaminate the entire computation domain.

Figures 7 and 8 are similar plots illustrating the excitation of the acoustic mode unstable solution in the PML. The Mach number and damping coefficient are $M_x = 0.5$, $M_y = 0.0$ and $\sigma = 1.5$. The initial disturbance consists of a pressure pulse given by,

$$
\begin{aligned}
&p = \rho = \exp\left[-(\ell n\, 2)\left(\frac{x^2+y^2}{9}\right)\right] \\
&u = v = 0.
\end{aligned}
\tag{11}
$$

The acoustic pulse generated by the initial disturbance propagates at a speed equal to the sound speed plus the flow velocity. Thus, the pulse leaves the small interior computation domain (50×50) very quickly. Figure 7a shows the pressure contours at $t = 140$. At this time, the acoustic pulse is gone. The contours are associated with the excited unstable waves of the acoustic mode. These unstable waves move at a slow speed. Figure 7b is at $t = 200$. On comparing figures 7a and 7b, it is evident that there is significant growth of the unstable waves. Upon reaching the outermost boundary of the computation domain the unstable waves are reflected back as short waves. This is illustrated in figure 7c. The reflected short waves propagate at ultrafast speed. They contaminate the computation domain in a short period of time as shown in figure 7d. Figure 8 shows the growth of the pressure waveform of the unstable acoustic mode waves in the PML before they reach the outer boundary of the computation domain. The measured growth rate has been found to agree with that calculated by the dispersion relation.

3. Development of a Stable PML

3.1. Artificial Selective Damping

To ensure practicality, the thickness of a PML would normally be limited to around 15 to 20 mesh spacings. For a PML with such a thickness, it is easy to show that if the transmitted wave from the computation domain is to be reduced by a factor of 10^5 in the presence of a subsonic mean flow, the damping coefficient σ of (1) should have a value of about

1.5. By solving the dispersion relations (2) and (3) numerically, it has been found that for $\sigma = 1.5$ the unstable wave solutions have only a modest rate of growth. Moreover, these waves, generally, have short wavelengths. Mild instabilities of this type can be effectively suppressed by the addition of artificial selective damping terms[12,14] to the discretized governing equations. The advantage of using artificial selective damping is that the damping is confined primarily to short waves. Thus, the perfectly matched condition is not adversely affected for the long waves (the physical waves) of the computation.

Consider the first equation of (1). Let (ℓ, m) be the spatial indices in the x- and y-directions. The semi-discretized form of this equation using the DRP scheme with artificial selective damping terms added to the right side is,

$$\frac{d}{dt}(u_1)_{\ell,m} + \sigma(u_1)_{\ell,m} + \sum_{j=-3}^{3} a_j[M_x(u_1 - u_2)_{\ell+j,m} + (p_1 + p_2)_{\ell+j,m}] \tag{12}$$

$$= -\frac{1}{R_\Delta}\sum_{j=-3}^{3} d_j[(u_1)_{\ell+j,m} + (u_2)_{\ell,j+m}]$$

where d_j's are the artificial selective damping coefficients[14] and $R_\Delta = a_\infty \frac{\Delta x}{\nu_e}$ is the artificial mesh Reynolds number. Terms similar to those on the right side of (12) are to be added to all the other discretized equations.

For the purpose of suppressing unstable solutions in the PML, we recommend the use of a damping curve with a slightly larger half-width then those given in ref. [14]. In this work, the following damping coefficients (half-width $= 0.35\pi$) are used.

$$\begin{aligned} d_0 &= 0.3705630354 \\ d_1 &= d_{-1} = -0.2411788110 \\ d_2 &= d_{-2} = 0.0647184823 \\ d_3 &= d_{-3} = -0.0088211899. \end{aligned} \tag{13}$$

The damping rate of the artificial selective damping terms can be found by taking the Fourier transform of the right side of (12) (see [12]). Let (α, β) be the transform variables in the (x, y)-plane. The rate of damping for wavenumber (α, β) is,

$$\text{damping rate} = \frac{1}{R_\Delta} D(\alpha, \beta) \tag{14}$$

where

$$D(\alpha, \beta) = \sum_{j=-3}^{3} d_j \left(e^{ij\alpha} + e^{ij\beta}\right). \tag{15}$$

Contours of the damping function $D(\alpha, \beta)$ in the $\alpha - \beta$-plane are shown in figure 9.

To demonstrate that suppression of the unstable solutions can be achieved by adding artificial selective damping terms to the discretized form of equation (1), let us consider the unstable solution with growth rate given by figure 3. On combining the growth rate of figure 3 and the damping rate of figure 9 with $R_\Delta = 1.421$, the resulting growth contours are shown in figure 10. Outside the dotted lines (wavenumber inside the vertical dotted lines corresponds to wavelengths too long to fit into a 15 mesh spacing PML) the combined effects result in damping of the waves. Thus all the instabilities of the PML equations are effectively suppressed.

3.2. Distributions of σ and R_Δ^{-1} in the PML

In the implementation of PML as an absorbing boundary condition, Hu[14] suggested letting σ vary spatially in the form,

$$\sigma = \sigma_m \left(\frac{d}{D}\right)^\lambda \tag{16}$$

where D is the thickness of the PML, d is the distance from the interface with the interior domain and λ is a constant. With the inclusion of artificial selective damping, we have found that the use of a well-designed smooth distribution of σ and R_Δ^{-1} at the interface region is important if the perfectly matched condition is to be maintained in the finite difference form of the system of equations.

Figure 11 shows a distribution of σ and R_Δ^{-1} we found to work well with the 7-point stencil DRP scheme. The R_Δ^{-1} curve is zero for the first two mesh points closest to the interface. It attends its full value $(R_\Delta^{-1})_{\max}$ at the 6^{th} mesh point. A cubic spline curve is used in the transition region. With this arrangement, the first point that artificial damping occurs is the third point from the interface. This allows the use of the 7-point symmetric damping stencil in the PML except the last three points at the outer boundary. For these points, the 5-point and the 3-point stencil[14] should be used instead.

The σ curve begins with the value $\sigma = 0$ at the fifth mesh point from the interface. The full value $\sigma_{\max}$ is reached at 8 mesh points further away. Again, a cubic spline curve is used in the transition

region. The choice of starting the σ curve at the fifth point is to ensure that the R_Δ^{-1} curve has attained its full value when σ becomes nonzero.

3.3. Numerical Examples

To demonstrate the effectiveness of using artificial selective damping terms to suppress the instabilities of the PML equations, the numerical examples of section 2.3 are reconsidered here. Artificial damping is now included in the simulations. Figure 12 shows the u-contours of the vorticity waves ($M_x = 0.3$, $M_y = 0.2$, $\sigma_m = 1.0$, $(R_\Delta^{-1})_{\max} = 1.0$) as they are convected from the interior domain to the PML. The vorticity wave packet is steadily damped. No sign of unstable waves of the type shown in figure 5 is detected. Figure 13 shows the corresponding waveform of u at a few selected times. It is clear that the pulse is damped continuously once it propagates into the PML. The case of the acoustic disturbance has also been repeated with similar results. Based on these findings, it is concluded that a stable PML can be developed by the inclusion of artificial selective damping. Such a PML performs very effectively as an absorbing boundary condition in an open domain.

4. PML in Ducted Environments

We will now consider the use of PML inside a circular duct of radius R. Dimensionless variables with respect to length scale R, velocity scale a_t (speed of sound at $r = R$), time scale $\frac{R}{a_t}$, density scale ρ_t (mean density at $r = R$) and pressure scale $\rho_t a_t^2$ will be used. The velocity components in the (x, r, ϕ) directions of a cylindrical coordinate system are denoted by (u, v, w). For an inviscid compressible flow, the most general mean flow (designated by an overbar) is

$$\overline{u} = \overline{u}(r), \quad \overline{v} = 0, \quad \overline{w} = \overline{w}(r), \quad \overline{\rho} = \overline{\rho}(r)$$

$$\overline{p} = -\int_r^1 \frac{\overline{\rho}\,\overline{w}^2}{r} dr + p_0. \tag{17}$$

Small amplitude disturbances superimposed on mean flow (17) are governed by the linearized Euler equations. They are,

$$\frac{\partial \rho}{\partial t} + \frac{1}{r}\frac{\partial}{\partial r}(\overline{\rho} v r) + \frac{\overline{w}}{r}\frac{\partial \rho}{\partial \phi} + \overline{u}\frac{\partial \rho}{\partial x} + \overline{\rho}\left(\frac{1}{r}\frac{\partial w}{\partial \phi} + \frac{\partial u}{\partial x}\right) = 0 \tag{18a}$$

$$\overline{\rho}\left[\frac{\partial v}{\partial t} + \overline{u}\frac{\partial v}{\partial x} + \frac{\overline{w}}{r}\frac{\partial v}{\partial \phi} - \frac{2\,\overline{w}\,w}{r}\right] - \rho\frac{\overline{w}^2}{r} = -\frac{\partial p}{\partial r} \tag{18b}$$

$$\overline{\rho}\left[\frac{\partial w}{\partial t} + \overline{u}\frac{\partial w}{\partial x} + v\frac{d\,\overline{w}}{dr} + \frac{\overline{w}}{r}\frac{\partial w}{\partial \phi} + \frac{\overline{w}\,v}{r}\right] = -\frac{1}{r}\frac{\partial p}{\partial \phi} \tag{18c}$$

$$\overline{\rho}\left[\frac{\partial u}{\partial t} + \overline{u}\frac{\partial u}{\partial x} + v\frac{d\,\overline{u}}{dr} + \frac{\overline{w}}{r}\frac{\partial u}{\partial \phi}\right] = -\frac{\partial p}{\partial x} \tag{18d}$$

$$\frac{\partial p}{\partial t} + \overline{u}\frac{\partial p}{\partial x} + \frac{\overline{w}}{r}\frac{\partial p}{\partial \phi} + \frac{\overline{\rho}\,\overline{w}^2}{r}v + \gamma\overline{p}\left[\frac{1}{r}\frac{\partial vr}{\partial r} + \frac{1}{r}\frac{\partial w}{\partial \phi} + \frac{\partial u}{\partial x}\right] = 0 \tag{18e}$$

where γ is the ratio of specific heats. The boundary condition at the duct wall is

$$r = 1, \qquad v = 0. \tag{19}$$

Solutions of (18) and (19) representing propagating wave modes in the duct may be written in the form,

$$\begin{bmatrix} \rho \\ u \\ v \\ w \\ p \end{bmatrix} = \mathrm{Re}\left\{ \begin{bmatrix} \widetilde{\rho}(r) \\ \widetilde{u}(r) \\ \widetilde{v}(r) \\ \widetilde{w}(r) \\ \widetilde{p}(r) \end{bmatrix} \exp[i(kx + m\phi - \omega t)] \right\}. \tag{20}$$

Substitution of (20) into (18) and (19) leads to the following eigenvalue problem.

$$\widetilde{\rho} + \frac{i}{\omega r}\frac{d}{dr}(\overline{\rho}\,\widetilde{v}\,r) - \frac{m\,\overline{w}}{\omega r}\widetilde{\rho} - \frac{k\,\overline{u}}{\omega}\widetilde{\rho} - \overline{\rho}\left(\frac{m}{\omega r}\widetilde{w} + \frac{k}{\omega}\widetilde{u}\right) = 0 \tag{21a}$$

$$\overline{\rho}\left[\left(1 - \frac{k}{\omega}\overline{u} - \frac{m\,\overline{w}}{\omega r}\right)\widetilde{v} - i\frac{2\,\overline{w}\,\widetilde{w}}{\omega r}\right] - \frac{i\,\widetilde{\rho}\,\overline{w}^2}{\omega r} = -\frac{i}{\omega}\frac{d\widetilde{p}}{dr} \tag{21b}$$

$$\overline{\rho}\left[\left(1 - \frac{k}{\omega}\overline{u} - \frac{m\,\overline{w}}{\omega r}\right)\widetilde{w} + \frac{i}{\omega}\widetilde{v}\frac{d\,\overline{w}}{dr} + \frac{i\,\overline{w}}{\omega r}\widetilde{v}\right]$$

$$= \frac{m}{\omega r}\widetilde{p} \tag{21c}$$

$$\overline{\rho}\left[\left(1-\frac{k}{\omega}\overline{u}-\frac{m\overline{w}}{\omega r}\right)\widetilde{u}+\frac{i}{\omega}\widetilde{v}\frac{d\overline{u}}{dr}\right] = \frac{k}{\omega}\widetilde{p} \tag{21d}$$

$$\left(1-\frac{k\overline{u}}{\omega}-\frac{m\overline{w}}{\omega r}\right)\widetilde{p}+\frac{i}{\omega}\frac{\overline{\rho}\,\overline{w}^2}{r}\widetilde{v}$$

$$+\gamma\overline{p}\left[\frac{i}{\omega r}\frac{d(\widetilde{v}\,r)}{dr}-\frac{m}{\omega r}\widetilde{w}-\frac{k}{\omega}\widetilde{u}\right]=0 \tag{21e}$$

$$r=1, \quad \widetilde{v}=0 \tag{22}$$

For a given azimuthal mode number m and frequency ω, k (the wavenumber) is the eigenvalue. Corresponding to an eigenvalue is an eigenvector $[\widetilde{\rho},\widetilde{u},\widetilde{v},\widetilde{w},\widetilde{p}]$, which describes the radial profile of the wave mode.

4.1. Perfectly Matched Condition in Ducted Flows

Suppose a perfectly matched layer is to be set up as a termination boundary of a computation domain inside a duct. By splitting the variables; e.g., $\rho = \rho_1 + \rho_2$, etc. in the standard manner, the PML equations corresponding to the linearized Euler equations ((18a) to (18e)) are,

$$\frac{\partial\rho_1}{\partial t}+\frac{1}{r}\frac{\partial}{\partial r}[\overline{\rho}(v_1+v_2)r]+\frac{\overline{w}}{r}\frac{\partial(\rho_1+\rho_2)}{\partial\phi}$$

$$+\frac{\overline{\rho}}{r}\frac{\partial(w_1+w_2)}{\partial\phi}=0 \tag{23a}$$

$$\frac{\partial\rho_2}{\partial t}+\sigma\rho_2+\overline{u}\frac{\partial(\rho_1+\rho_2)}{\partial x}$$

$$+\overline{\rho}\frac{\partial(u_1+u_2)}{\partial x}=0 \tag{23b}$$

$$\overline{\rho}\left[\frac{\partial v_1}{\partial t}+\frac{\overline{w}}{r}\frac{\partial(v_1+v_2)}{\partial\phi}-\frac{2\,\overline{w}(w_1+w_2)}{r}\right]$$

$$-(\rho_1+\rho_2)\frac{\overline{w}^2}{r}=-\frac{\partial}{\partial r}(p_1+p_2) \tag{23c}$$

$$\overline{\rho}\left[\frac{\partial v_2}{\partial t}+\sigma v_2+\overline{u}\frac{\partial(v_1+v_2)}{\partial x}\right]=0 \tag{23d}$$

$$\overline{\rho}\left[\frac{\partial w_1}{\partial t}+(v_1+v_2)\frac{d\overline{w}}{dr}+\frac{\overline{w}}{r}\frac{\partial(w_1+w_1)}{\partial\phi}\right.$$

$$\left.+\frac{\overline{w}}{r}(v_1+v_2)\right]=-\frac{1}{r}\frac{\partial(p_1+p_2)}{\partial\phi} \tag{23e}$$

$$\overline{\rho}\left[\frac{\partial w_2}{\partial t}+\sigma w_2+\overline{u}\frac{\partial(w_1+w_2)}{\partial x}\right]=0 \tag{23f}$$

$$\overline{\rho}\left[\frac{\partial u_1}{\partial t}+(v_1+v_2)\frac{d\overline{u}}{dr}+\frac{\overline{w}}{r}\overline{u}\frac{\partial(u_1+u_2)}{\partial\phi}\right]$$

$$=0 \tag{23g}$$

$$\overline{\rho}\left[\frac{\partial u_2}{\partial t}+\sigma u_2+\overline{u}\frac{\partial(u_1+u_2)}{\partial x}\right]$$

$$=-\frac{\partial(p_1+p_2)}{\partial x} \tag{23h}$$

$$\frac{\partial p_1}{\partial t}+\frac{\overline{w}}{r}\frac{\partial(p_1+p_2)}{\partial\phi}+\frac{\overline{\rho}\,\overline{w}^2}{r}(v_1+v_2)$$

$$+\gamma\overline{p}\left[\frac{1}{r}\frac{\partial r(v_1+v_2)}{\partial r}+\frac{1}{r}\frac{\partial(w_1+w_2)}{\partial\phi}\right]$$

$$=0 \tag{23i}$$

$$\frac{\partial p_2}{\partial t}+\sigma p_2+\overline{u}\frac{\partial(p_1+p_2)}{\partial x}+\gamma\overline{p}\frac{\partial(u_1+u_2)}{\partial x}$$

$$=0 \tag{23j}$$

where σ is the damping coefficient in the PML. The boundary condition is

$$r=1, \qquad v_1+v_2=0. \tag{24}$$

In the PML, the duct modes are represented by solutions of the form (similar to (20)),

$$\rho_1(r,\phi,x,t)=\mathrm{Re}\left[\widehat{\rho}_1(r)e^{i(\kappa x+m\phi-\omega t)}\right], \tag{25}$$

etc., where κ is the wavenumber. On substituting (25) into (23) and (24) and on defining

$$\begin{aligned}\widehat{\rho}&=\widehat{\rho}_1+\widehat{\rho}_2\\ \widehat{u}&=\widehat{u}_1+\widehat{u}_2\\ \widehat{v}&=\widehat{v}_1+\widehat{v}_2\\ \widehat{w}&=\widehat{w}_1+\widehat{w}_2\\ \widehat{p}&=\widehat{p}_1+\widehat{p}_2\end{aligned} \tag{26}$$

it is straightforward to find that the duct modes in the PML are given by the solutions of the following eigenvalue problem.

$$\widehat{\rho}+\frac{i}{\omega r}\frac{d}{dr}(\overline{\rho}\,\widehat{v}\,r)-\frac{m\,\overline{w}}{\omega r}\,\widehat{\rho}-\frac{\kappa\,\overline{u}}{\omega+i\sigma}\,\widehat{\rho}$$

$$-\overline{\rho}\left(\frac{m}{\omega r}\,\widehat{w}+\frac{\kappa}{\omega+i\sigma}\,\widehat{u}\right)=0 \qquad (27a)$$

$$\overline{\rho}\left[\left(1-\frac{\kappa}{\omega+i\sigma}\,\overline{u}-\frac{m\,\overline{w}}{\omega r}\right)\widehat{v}-i\frac{2\,\overline{w}\,\widehat{w}}{\omega r}\right]$$

$$-\frac{i\,\widehat{\rho}\,\overline{w}^2}{\omega r}=-\frac{i}{\omega}\frac{d\,\widehat{p}}{dr} \qquad (27b)$$

$$\overline{\rho}\left[\left(1-\frac{\kappa}{\omega+i\sigma}\,\overline{u}-\frac{m\,\overline{w}}{\omega r}\right)\widehat{w}+\frac{i}{\omega}\,\widehat{v}\,\frac{d\,\overline{w}}{dr}\right.$$

$$\left.+\frac{i\,\overline{w}}{\omega r}\,\widehat{v}\right]=\frac{m}{\omega r}\,\widehat{p} \qquad (27c)$$

$$\overline{\rho}\left[\left(1-\frac{\kappa}{\omega+i\sigma}\,\overline{u}-\frac{m\,\overline{w}}{\omega r}\right)\widehat{u}\right.$$

$$\left.+\frac{i}{\omega}\,\widehat{v}\,\frac{d\,\overline{u}}{dr}\right]=\frac{\kappa}{\omega+i\sigma}\,\widehat{p} \qquad (27d)$$

$$\left(1-\frac{\kappa\,\overline{u}}{\omega+i\sigma}-\frac{m\,\overline{w}}{\omega r}\right)\widehat{p}+\frac{i}{\omega}\frac{\overline{\rho}\,\overline{w}^2}{r}\,\widehat{v}$$

$$+\gamma\,\overline{p}\left[\frac{i}{\omega r}\frac{d(\widehat{v}\,r)}{dr}-\frac{m}{\omega r}\,\widehat{w}-\frac{\kappa}{\omega+i\sigma}\,\widehat{u}\right]$$

$$=0. \qquad (27e)$$

The boundary condition is

$$r=1, \qquad \widehat{v}=0. \qquad (28)$$

The eigenvalue is κ. On comparing eigenvalue problem (21) and (22) with eigenvalue problem (27) and (28), it is immediately clear that they are the same if $\frac{k}{\omega}$ in (21) is replaced by $\frac{\kappa}{\omega+i\sigma}$. Thus the eigenvalues are related by

$$\kappa=k\left(1+\frac{i\sigma}{\omega}\right). \qquad (29)$$

On the other hand, the eigenvectors are identical. The fact that the eigenvectors of a duct mode in the interior region of the computation domain is the same as that in the PML assures that there is perfect matching. That is, a propagating duct mode incident on the PML will be totally transmitted into the PML without reflection. If the mean flow is nonuniform, some of the duct modes may involve Kelvin-Helmholtz or other types of flow instability waves. However, the perfectly matched condition is still valid for these waves.

4.2. The Case of Uniform Mean Flow

From (25) and (29), the transmitted wave mode has the form

$$[\widehat{\rho}(r),\widehat{u}(r),\widehat{v}(r),\widehat{w}(r),\widehat{p}(r)]\,e^{i[k(1+\frac{i\sigma}{\omega})x+m\phi-\omega t]}. \qquad (30)$$

If the wave mode is nondispersive, then $\frac{k}{\omega}$, the inverse of the phase velocity, is positive for waves propagating in the x-direction and negative in the opposite direction. For these nondispersive waves, the transmitted waves are spatially damped; a condition needed by the PML if it is to serve as an absorbing boundary condition. However, inside a duct, the wave modes are dispersive. The direction of propagation is given by the group velocity $\frac{d\omega}{dk}$. We will now show that in the presence of a uniform mean flow there is a band of acoustic duct modes for which the group velocity and the phase velocity have opposite signs. Therefore, for this band of waves, the transmitted waves would grow spatially instead of being damped.

By eliminating all the other variables in favor of $\widetilde{p}(r)$, it is straightforward to find, in the case of a uniform mean flow of Mach number M, (21) and (22) reduce to the following simple eigenvalue problem.

$$\frac{d^2\widetilde{p}}{dr^2}+\frac{1}{r}\frac{d\widetilde{p}}{dr}+\left[(\omega-Mk)^2-k^2-\frac{m^2}{r^2}\right]\widetilde{p}=0 \qquad (31)$$

$$r=1, \qquad \frac{d\widetilde{p}}{dr}=0. \qquad (32)$$

The eigenfunction is

$$\widetilde{p}=J_m(\lambda_{mn}r) \qquad (33)$$

where $J_m(\ \ )$ is the m^{th} order Bessel function and λ_{mn} is the n^{th} root of

$$J'_m(\lambda_{mn})=0. \qquad (34)$$

By substitution of (33) into (31), it is found that the dispersion relation or eigenvalue equation for the $(m,n)^{\text{th}}$ acoustic duct mode is

$$(\omega-Mk)^2-k^2=\lambda_{mn}^2. \qquad (35)$$

The axial wavenumber of the mode at frequency ω are given by the solution of (35). They are,

$$k_{\pm} = \frac{-\omega M \pm [\omega^2 - (1-M^2)\lambda_{mn}^2]^{\frac{1}{2}}}{(1-M^2)}. \qquad (36)$$

The group velocity of the duct mode may be determined by implicit differentiation of (35). This gives,

$$\frac{d\omega}{dk} = \frac{\pm[\omega^2 - (1-M^2)\lambda_{mn}^2]^{\frac{1}{2}}(1-M^2)}{\omega \mp M[\omega^2 - (1-M^2)\lambda_{mn}^2]^{\frac{1}{2}}}. \qquad (37)$$

In (37), the upper sign corresponds to $k = k_+$ and the lower sign corresponds to $k = k_-$. For subsonic mean flow, clearly $\frac{d\omega}{dk} > 0$ for $k = k_+$ and $\frac{d\omega}{dk} < 0$ for $k = k_-$. Therefore, the downstream propagating waves have wavenumber given by $k = k_+$, while the upstream propagating waves have wavenumber equal to k_-.

From (37), it is easy to show that for $(1 - M^2)^{\frac{1}{2}}\lambda_{mn} < \omega < \lambda_{mn}$ the phase velocity $\frac{k_{\pm}}{\omega}$ is negative although the group velocity is positive. According to (29), for waves in this frequency band, the transmitted wave in the PML will amplify spatially. This renders the PML useless as an absorbing layer except for $M = 0$. In the absence of a mean flow normal to the PML ($M = 0$), k_+ will not be negative by (36). Thus, the transmitted waves in the PML are evanescent. For this special condition, the PML can again be used as an absorbing boundary condition.

4.3. Numerical Examples

To demonstrate that a PML in a ducted environment actually supports a band of amplifying wave modes, a series of numerical simulations has been carried out. In the simulations, a uniform mesh with $\Delta x = \Delta r = 0.04$ covering the entire computation domain from $x = -6.0$ to $x = 12.0$ is used. The PML in the upstream direction begins at $x = -3.0$ and extends to $x = -6.0$. In the downstream direction, the PML occupies the region from $x = 3.0$ to $x = 12.0$. The dimensionless damping constant (nondimensionalized by $\frac{a_\infty}{R}$) σ is set equal to 25.0. The results of two simulations, one with a mean flow Mach number 0.4, the other with no mean flow are reported below.

For convenience, only the axisymmetric duct modes are considered. The computation uses the 7-point stencil DRP scheme[13]. The acoustic disturbances in the computation domain is initiated by a pressure pulse located at $x = 0$ and $r = 0.5$. The initial condition is,

$$t = 0, \quad u = v = 0,$$
$$p = \rho = \exp\left[-(\ell n\, 2)\frac{(x^2 + (r-0.5)^2)}{16}\right]. \qquad (38)$$

Figure 14 shows the time evolution of the acoustic disturbance inside the computation domain at $M = 0.4$. Specifically, the pressure waveforms along the line $r = 0.38$ are shown at $t = 10$, 13, 15 and 16. As can be seen, once the pressure pulse is released, it spreads out and propagates upstream and downstream. Figure 14a indicates that at time $t = 10$ the front of the acoustic disturbance has just entered the PML in the downstream direction. There is no evidence of wave reflection at the interface between the PML and the interior computation domain. The transmitted wave grows spatially as shown in figure 14b. The amplitude of the transmitted wave increases steadily as they propagate across the PML. This is shown in figures 14c and 14d. When the amplified waves reach the outermost boundary of the PML, large amplitude spurious waves are reflected back. This quickly contaminates the entire computation domain.

Figure 15 shows the same simulation except that there is no mean flow. In the absence of a mean flow, the PML acts as an absorbing layer. Figure 15a shows the entry of the acoustic pulse into the downstream PML. Figures 15b to 15d show the damping of the acoustic pulse in time in the PML. The slowest components to decay are the long waves. This is in agreement with the analysis of the previous section.

5. Concluding Remarks

In this paper, we have shown that the application of PML as an absorbing boundary condition for the linearized Euler equations works well as long as there is no mean flow in the direction normal to the layer. For open domain problems, the PML equations, in the presence of a subsonic mean flow normal to the layer, support unstable solutions. The growth rate of the unstable solutions is, however, not large. These unstable solutions can, generally, be suppressed by the addition of artificial selective damping. In the case of a ducted environment, we find that because of the highly dispersive nature of the duct modes, a band of the transmitted waves in the PML amplifies instead of being damped. This seemingly renders the PML totally ineffective as an absorbing boundary condition.

One of the important advantages of using an absorbing boundary condition instead of other numerical boundary treatments is that the boundary of the computation domain may be put much closer to the source of disturbances. In this way, a smaller computation domain may be used in a numerical simulation. For open domains, such an absorbing boundary condition can be developed by the use of PML with artificial selective damping terms. Unfortunately, the same is not possible for internal ducted flow. An effective numerical anechoic termination for ducted domains has yet to be developed.

Acknowledgement

This work was supported by NASA Langley Research Grant NAG 1–1776.

References

1. J.P. BERENGER, A perfectly matched layer for the absorption of electromagnetic waves, J. Comput. Phys. **114**, 185 (1994).
2. J.P. BERENGER, Three dimensional perfectly matched layer for the absorption of electromagnetic waves, J. Comput. Phys. **127**, 363 (1996).
3. F.D. HASTINGS, J.B. SCHNEIDER AND S.L. BROSCHAT, Application of the perfectly matched layer (PML) absorbing boundary condition to elastic wave propagation, J. Acoust. Soc. Amer. **100**, 3061 (1996).
4. F.Q. HU, On absorbing boundary conditions for linearized Euler equations by a perfectly matched layer, J. Comput. Phys. **129**, 201 (1996).
5. F.Q. HU, On perfectly matched layer as an absorbing boundary condition, AIAA paper 96–1664 (1996).
6. M. HAYDER, F.Q. HU, AND Y.M. HUSSAINI, Toward perfectly matched boundary conditions for Euler equations, AIAA paper 97–2075 (1997).
7. F.Q. HU AND J.L. MANTHEY, Application of PML absorbing boundary conditions to the benchmark problems of computational aeroacoustics, Proc. Second Comput. Aeroacoustics Workshop on Benchmark Problems, NASA CP–3352, 119 (1997).
8. P.M. MORSE AND K.U. INGARD, Theoretical Acoustics (McGraw Hill, New York, 1968).
9. W. EVERSMAN, Theoretical models for duct acoustic propagation and radiation, Chapter 13, pp. 101–163, in Aeroacoustics of Flight Vehicles: Theory and Practice, Vol. 2, NASA RP–1258 (1991).
10. C.K.W. TAM, Advances in numerical boundary conditions for computational aeroacoustics, AIAA Paper 97–1774 (1997), to appear in J. Comput. Acoustics.
11. S. ABARBANEL AND D. GOTTLIEB, A mathematical analysis of the PML method, J. Comput. Phys. **134**, 357 (1997).
12. C.K.W. TAM, J.C. WEBB AND Z. DONG, A study of the short wave components in computational acoustics, J. Comput. Acoustics **1**, 1 (1993).
13. C.K.W. TAM AND J.C. WEBB, Dispersion-Relation-Preserving finite difference schemes for computational acoustics, J. Comput. Phys. **107**, 262 (1993).
14. C.K.W. TAM, Computational Aeroacoustics: Issues and Methods, AIAA J. **33**, 1788 (1995).

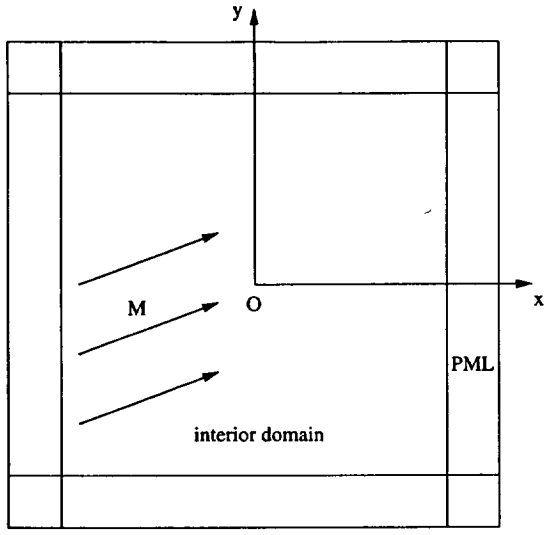

Figure 1. Two dimensional computation domain with Perfectly Matched Layers as boundaries.

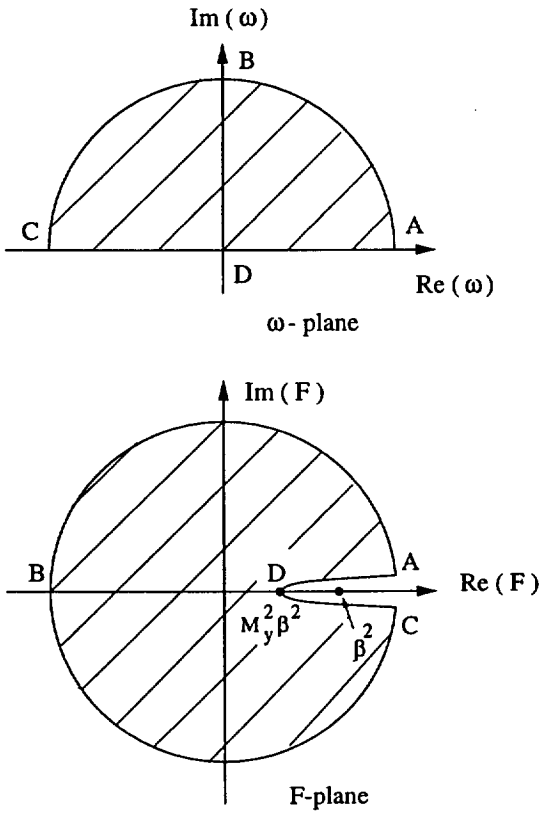

Figure 2. The image of the upper half ω-plane in the F-plane.

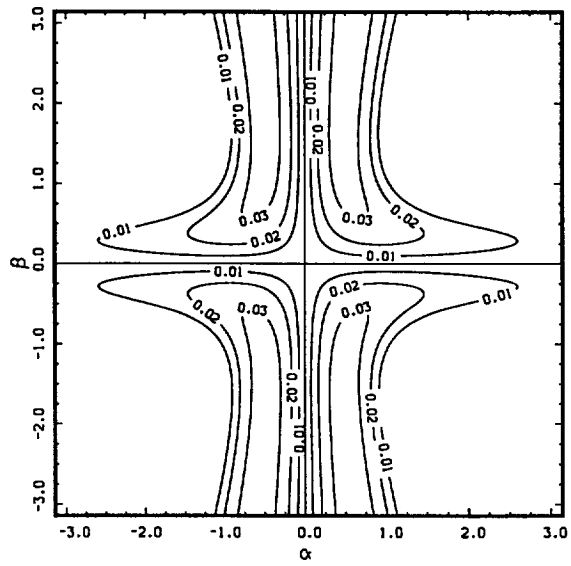

Figure 3. Contours of the growth rate of the most unstable wave (acoustic mode) in the $\alpha - \beta$ plane. $M_x = 0.3$, $M_y = 0.0$, $\sigma = 1.5$.

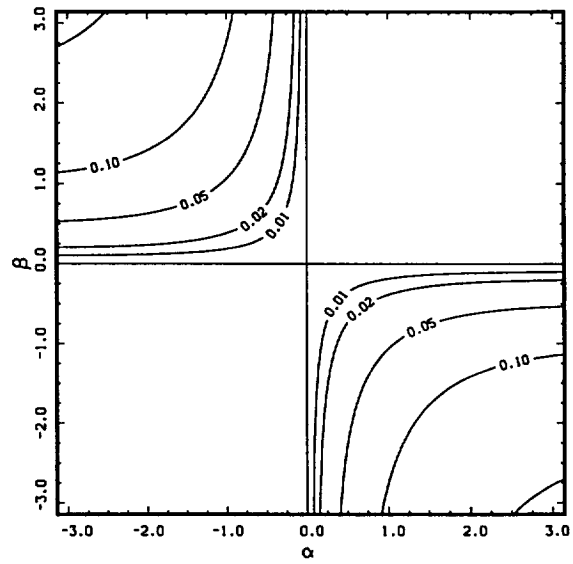

Figure 4. Contours of the growth rate of the most unstable vorticity wave in the $\alpha - \beta$ plane. $M_x = 0.3$, $M_y = 0.2$, $\sigma = 1.0$.

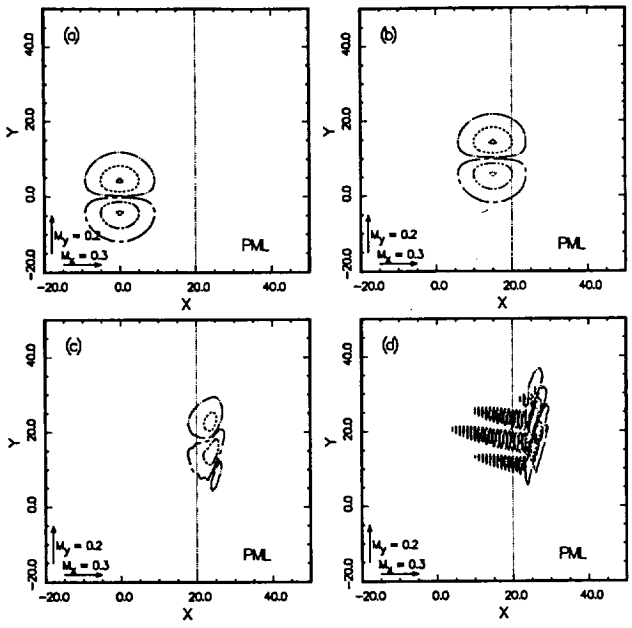

Figure 5. Numerical simulation showing the generation and propagation of unstable vorticity-mode waves in the PML. $M_x = 0.3$, $M_y = 0.2$, $\sigma_m = 1.0$. (a) $t = 0$, (b) $t = 50$, (c) $t = 90$, (d) $t = 130$. Contours of the u velocity component. ——— 0.1, - - - - - 0.05, — · — 0.01, — - — -0.01, - - ——— -0.05, ····· -0.1.

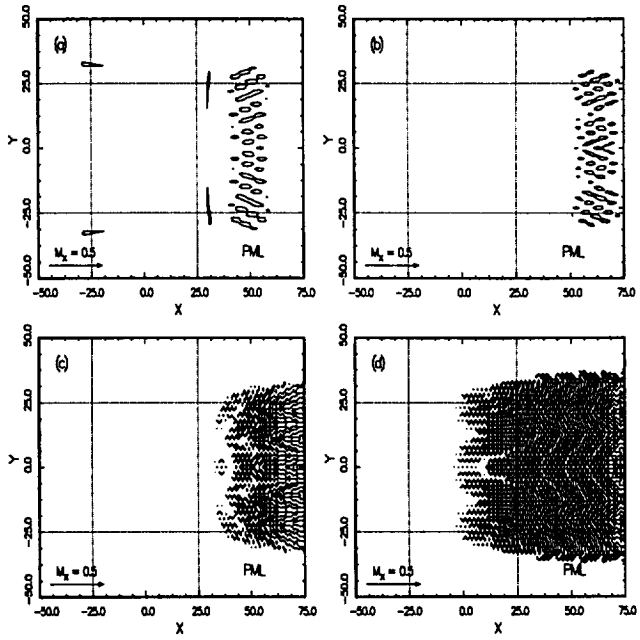

Figure 7. Numerical simulation showing the generation and propagation of unstable acoustic-mode waves in the PML. $M_x = 0.5$, $M_y = 0.0$, $\sigma_m = 1.5$. Contours of pressure.
(a) $t = 140$, —— $p = 10^{-4}$ (b) $t = 200$, —— $p = 5.\ 10^{-3}$
(c) $t = 260$, —— $p = 5.\ 10^{-2}$ (d) $t = 300$, —— $p = 5.\ 10^{-2}$

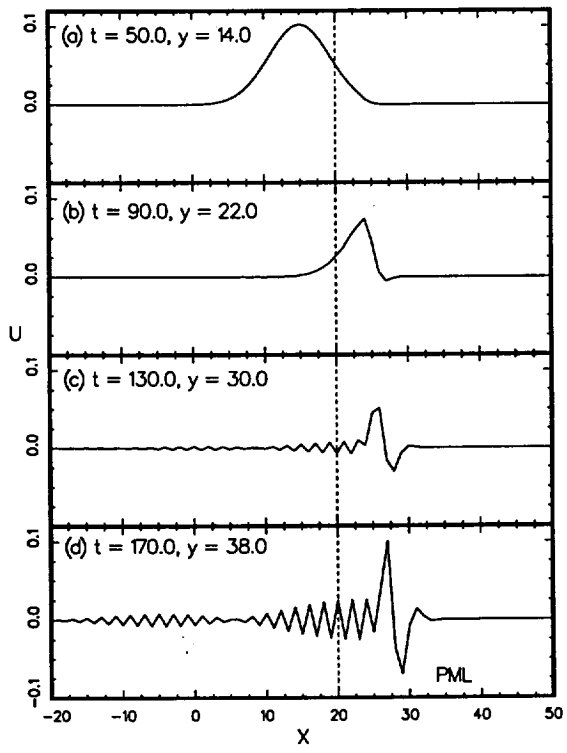

Figure 6. Waveforms of u showing the generation of unstable vorticity-mode waves excited by vorticity waves convected from the interior computation domain to the PML and the subsequent contamination of the interior computation domain. $M_x = 0.3$, $M_y = 0.2$, $\sigma_m = 1.0$.

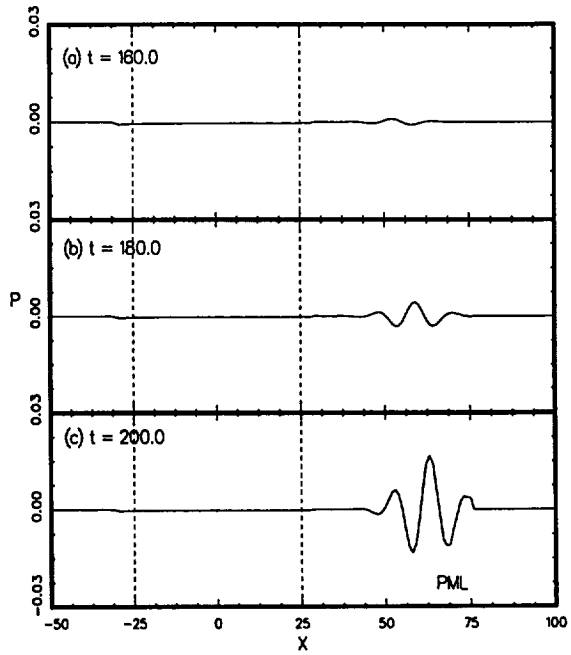

Figure 8. Waveforms of pressure along $y = 0$ showing the generation of unstable acoustic-mode waves in the PML excited by acoustic disturbances from the computation domain. $M_x = 0.5$, $M_y = 0.0$, $\sigma_m = 1.5$.

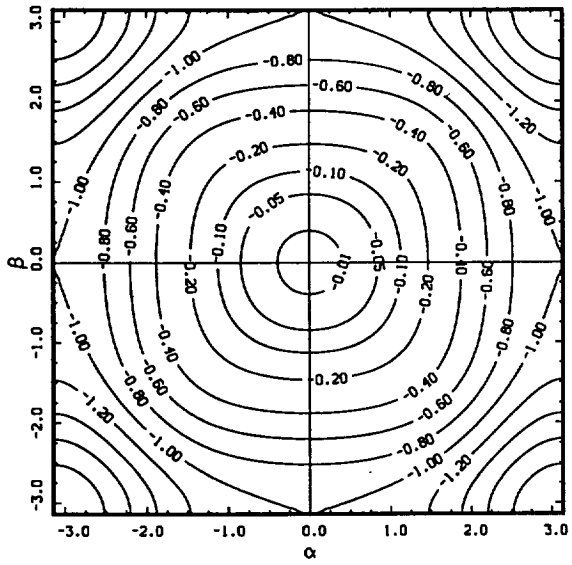

Figure 9. Contours of constant $D(\alpha, \beta)$ in the $\alpha-\beta$ plane. Damping coefficients d_j's are given by (13).

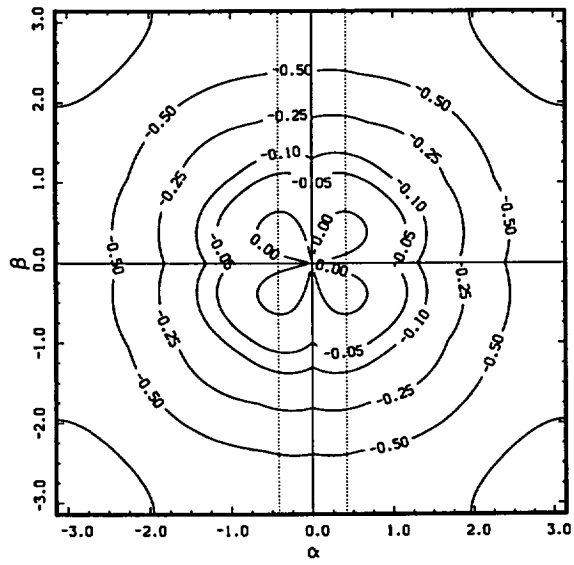

Figure 10. Contours of combined growth and damping rates. $M_x = 0.3$, $M_y = 0.0$, $\sigma = 1.5$, $R_\Delta = 1.42$. Damping coefficients d_j's are given by (13).

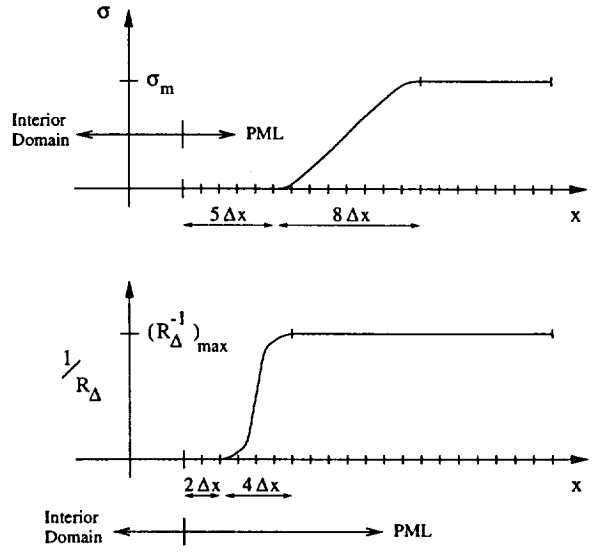

Figure 11. Distributions of σ and R_Δ^{-1} in a 20 mesh spacings PML.

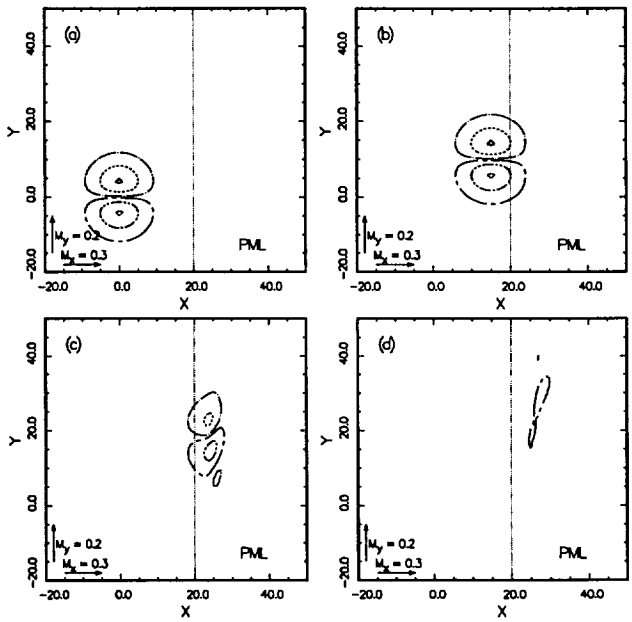

Figure 12. Damping of a vorticity wave packet in the PML including artificial selective damping terms. $M_x = 0.3$, $M_y = 0.2$, $\sigma_m = 1.0$, $(R_\Delta^{-1})_{max} = 1.0$. (a) $t = 0$, (b) $t = 50$, (c) $t = 90$, (d) $t = 170$. Contours of the u velocity component. ——— 0.1, - - - - - 0.05, — · — 0.01, — - — -0.01, - - ——— -0.05, ····· -0.1.

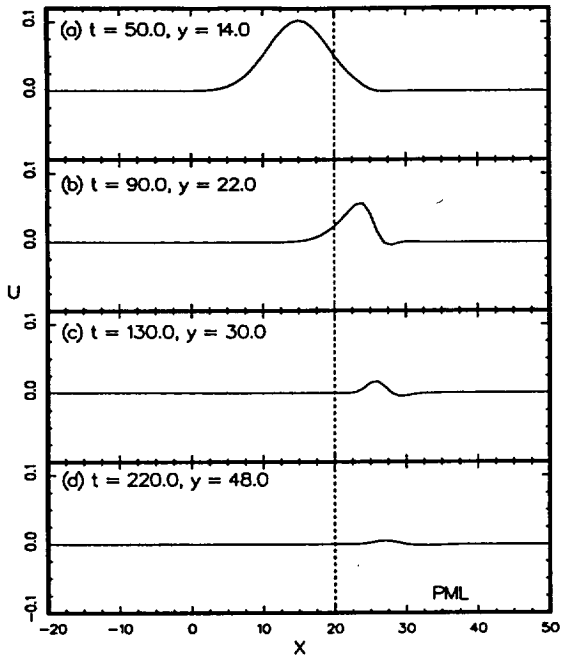

Figure 13. Waveforms showing the damping of a vorticity wave packet as it is convected into a PML with artificial selective damping terms. $M_x = 0.3$, $M_y = 0.2$, $\sigma_m = 1.0$, $(R_\Delta^{-1})_{max} = 1.0$.

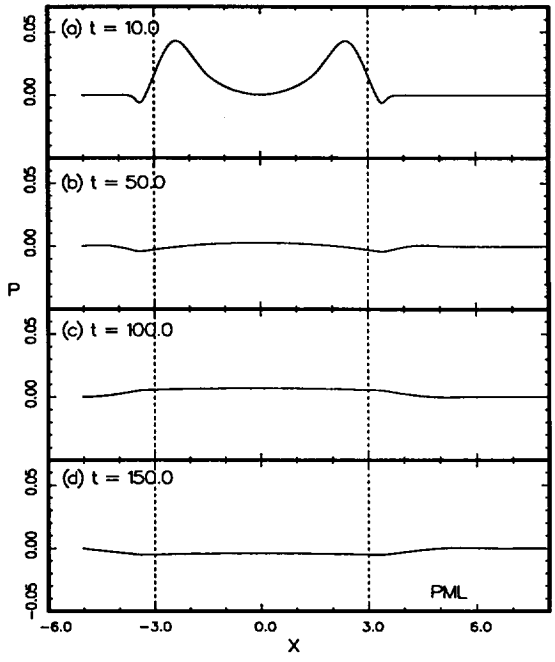

Figure 15. Pressure waveforms along the line $r = 0.38$ of a circular duct without mean flow showing the damping of an acoustic pulse in the PML. $\Delta x = \Delta r = \frac{R}{25}$, $\sigma_m = 25.0$.

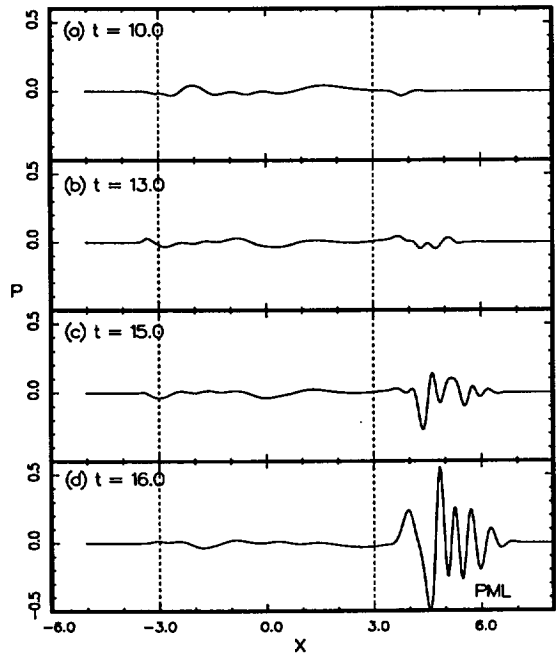

Figure 14. Pressure waveforms along the line $r = 0.38$ of a circular duct with uniform mean flow at Mach 0.4 showing the excitation and growth of the unstable solution in the PML by an acoustic pulse. $\Delta x = \Delta r = \frac{R}{25}$, $\sigma_m = 25.0$.

THE EFFECT OF NOZZLE GEOMETRY ON THE NOISE OF HIGH-SPEED JETS

Christopher K.W. Tam

Department of Mathematics, Florida State University
Tallahassee, FL 32306-4510 USA

ABSTRACT

This paper examines the effectiveness of jet noise reduction by the use of different nozzle exit geometry. Since there will be thrust loss associated with a nozzle of complex geometry, consideration is confined to practical configurations with reasonably small thrust loss. In this study, only jets with a single stream are considered. The nozzle configurations examined are circular, elliptic and rectangular. Included also are plug nozzles as well as a suppressor nozzle. It is shown that the measured turbulent mixing noise of the jets from these nozzles consists of two independent components. The noise spectrum of each component is found to fit the shape of a seemingly universal similarity spectrum. It is also found that the maximum levels of the fitted noise power spectra of the jets are nearly the same. This finding suggests that nozzle geometry modification may not be an effective method for jet noise suppression.

1. INTRODUCTION

Reducing high-speed jet noise is currently a high priority research and development effort of the aircraft industry. Despite many years of jet noise research, noise reduction is a highly empirical endeavor. Since the early work of Westly and Lilley[1] many attempts have been made to modify the shape of the nozzle exit in the belief that this would reduce the turbulence intensity of the jet leading to a reduction in the radiated noise. On following this concept, plug nozzles, corrugated nozzles as well as nozzles with multi-chute elements have been introduced for noise suppression purpose.

The objective of this paper is to examine the effectiveness of jet noise reduction by nozzle exit geometry modification. Of course, there will be thrust loss in using a nozzle with complex geometry. Our consideration is, therefore, confined to practical geometries for which the thrust loss is reasonably small. In order to focus attention

on nozzle geometry alone, we will only consider jets formed by a single stream. Multi-stream jets, invariably, would introduce thermodynamic and other flow parameters as variables. Under this circumstance, a simple statement on the effectiveness of nozzle configuration for noise suppression cannot be easily made.

In Section 2 of this paper, the effect of nozzle geometry on the turbulent mixing processes in jets is discussed. For high-speed jets the mixing process is influenced only by upstream events. Thus the normal expectation is that the nozzle exit configuration would exert considerable influence on the development of the large and fine scale turbulence of the jet flow and hence its noise. In Section 3, turbulent mixing noise data from a variety of nozzles will be examined and analyzed. It will be shown that the noise level is, to a large extent, insensitive to the nozzle shape. This is true even for jets embedded in open wind tunnel flows simulating forward flight effects. This result seems to suggest that modification of a nozzle exit configuration may not be an effective method for noise suppression.

2. NOZZLE GEOMETRY AS AN INITIAL CONDITION

Tam and Chen[3], based on their observation of the noise directivity and spectrum measurements of Seiner *et al.*[4], were the first to clearly suggest that turbulent mixing noise from high-speed jets is made up of two components. One component is in the form of Mach wave radiation generated by the large turbulence structures of the jet flow. This component radiates only in the downstream direction. The other component is generated by the fine scale turbulence of the jet. The radiated noise has a more uniform directivity. Experimental confirmation of the existence of the two noise components was not available until the recent investigation of Tam, Golebiowski and Seiner[2]. By analyzing the entire data bank of axisymmetric jet noise spectra measured in the Jet Noise Laboratory of the NASA Langley Research Center, they were able to extract the shapes of two self-similar spectra from the data. They then demonstrated that all the noise spectra were made up of a combination of the two similarity spectra. Let S be the noise power spectrum (S has the dimensions of pressure squared per unit frequency) then S can be expressed in the following similarity form,

$$S = \left[AF\left(\frac{f}{f_L}\right) + BG\left(\frac{f}{f_F}\right)\right]\left(\frac{D_j}{r}\right)^2 \tag{1}$$

where $F\left(\frac{f}{f_L}\right)$ and $G\left(\frac{f}{f_F}\right)$ are the similarity spectra of the large turbulence structure noise and the fine scale turbulence noise respectively. f_L is the frequency at the peak of the large turbulence structures noise spectrum and f_F is the frequency at the peak of the fine scale turbulence noise spectrum. The spectrum functions are normalized such that $F(1) = G(1) = 1$. In equation (1), A and B are the amplitudes of the independent spectra. They have the same dimensions as S. D_j is the fully expanded jet diameter and r is the distance between the noise measurement point and the nozzle exit. The amplitudes A and B and the peak frequencies f_L and f_F are functions of the jet operating parameters $\frac{v_j}{a_\infty}$, $\frac{T_r}{T_\infty}$ and the direction of radiation χ (measured from the jet inlet). v_j and a_∞ are the jet velocity and the ambient sound speed. T_r and T_∞ are the reservoir and ambient temperature. One remarkable feature of the similarity spectra is that they fit the data well regardless of jet velocity, jet temperature, direction

of radiation, and whether the jet is perfectly or imperfectly expanded (in the case of supersonic jets). These spectra are used extensively in the present investigation.

In high-speed jet flows, there is practically very little upstream influence. Thus the turbulence level near the end of the core region, where most of the jet noise is generated, is affected primarily by the mixing processes upstream and the conditions at the nozzle exit. From this point of view, the nozzle geometry may be regarded as an initial condition on the spatial evolution of the jet velocity profile and the turbulence intensity and spectral content downstream. For noise suppression purposes, the crucial question to ask is how sensitive the turbulence level of the jet flow near the end of the potential core is to the initial condition at the nozzle exit. There is no question that by changing nozzle geometry the entrainment flow and hence jet turbulence in the region immediately downstream of the nozzle exit is affected. However, turbulent mixing is a highly nonlinear process. It is known, nonlinear process can lead to the same asymptotic state regardless of initial conditions. (For a discussion of the lack of influence of initial conditions on self-similar turbulent flows, see the work of Tam and Chen[5].) For high Reynolds number jet flows, it is possible that a jet issued from a noncircular nozzle evolves quickly into a more or less axisymmetric jet before the end of the core is reached. In such a case, the radiated noise would be similar to that of a circular jet both in intensity and spectral content. In the next section, it will be shown that this appears to be the case.

3. EVALUATION AND COMPARISONS OF DATA

Supersonic jet noise data from two sources are used in the present study. The first set of data is taken from the data bank of the Jet Noise Laboratory of the NASA Langley Research Center. This set of data consists of noise spectra from a Mach 2 aspect ratio 3 elliptic jet and a Mach 2 aspect ratio 7.6 rectangular jet. These are high quality data; comparable to those used in the work of Tam, Golebiowski and Seiner[2].

The second set of data is taken from the published measurements of Yamamoto *et al.*[6]. In this series of experiments, six nozzles are used. They include a conical nozzle, a convergent-divergent (C-D) round nozzle, a convergent annular plug nozzle, a C-D annular plug nozzle, a 20-chute annular plug suppressor nozzle with convergent flow segment terminations and a 20-chute annular plug suppressor nozzle with C-D flow element terminations. The noise spectra of the jet from the fifth nozzle, however, are strongly different from the same configuration suppressor nozzle but with C-D flow element terminations and the other nozzles. Without knowing the cause of the difference, it is decided to ignore the data associated with this nozzle.

3.1 COMPARISONS WITH SIMILARITY NOISE SPECTRA

Figure 1 shows direct comparisons between the measured elliptic and rectangular jet noise spectra at Mach 2 and $\frac{T_r}{T_\infty} = 1.8$ from the NASA Langley Research Center and the similarity spectrum for the large turbulence structures noise of Tam *et al.*[2] at $\chi = 150$ deg. The elliptic jet noise data are measured on three planes containing the jet axis. One is on the minor axis plane, one on a plane at 58 degrees to the minor axis plane and the third on the major axis plane. They are the top three curves in the figure. The bottom two curves are from the rectangular jet noise data measured on the minor and major axis planes. As can be seen, there is good agreement between the

measured spectrum shapes and the similarity noise spectrum (the $F(\frac{f}{f_L})$ function of equation (1)). This is so despite the fact that the nozzle geometries are very different.

Comparisons between the measured spectra at $\chi = 90$ deg. and the similarity noise spectrum or the fine scale turbulence noise (the $G(\frac{f}{f_F})$ function of equation (1)) for the elliptic and rectangular jets are given in Figure 2. Again, the top three curves are those of the elliptic jet and the bottom two curves are of the rectangular jet measured on the same azimuthal planes as in Figure 1. It is evident that there is good agreement overall regardless of nozzle shapes.

Figure 3 shows the noise spectrum shapes of the Yamamoto *et al.* data[6] at $\chi = 150$ deg. The jet velocity in each case is very close to 2420 ft/sec and the total temperature is approximately 1715 deg. Rankine. The four spectra are (from the top down) from the C-D round nozzle, the convergent annular plug nozzle, the C-D annular plug nozzle and the 20-chute annular suppressor nozzle. The data from the conical nozzle is nearly the same as the C-D round nozzle and is, therefore, not displayed. The full curves are the similarity noise spectrum (the $F(\frac{f}{f_L})$ function) of Tam *et al.*[2]. On ignoring the very low frequency part of the noise spectrum, it is clear that the agreement between the measured data and the similarity spectrum is good for all the cases.

Figure 4 shows similar comparisons as in Figure 3 but at $\chi = 90$ deg. By comparing the several spectra shown, the facility noise contamination at low frequencies can be readily detected. The full curves are the similarity spectrum given by the $G(\frac{f}{f_F})$ function. Overall, there is again good fit between the data and the similarity spectrum.

3.2 COMPARISONS OF MAXIMUM SOUND PRESSURE LEVELS

To assess whether nozzle geometry has significant influence on high-speed jet noise, we compare the sound pressure levels at the peaks of the fitted noise spectra, $SPL_{\max}$, in dB/Hz at $r = 100D_j$ from the various jets with the level of the simple circular C-D nozzle. The results are shown in Tables 1 to 4.

Table 1 compares the $SPL_{\max}$ of the elliptic jet at temperature ratio $(\frac{T_r}{T_\infty})$ of 1.0, 1.37, 1.80 and 2.27 at jet Mach number 1.98 with the corresponding values of a circular jet. We have chosen the microphone measurements at $\chi = 150$ deg. to characterize the large turbulence structures noise component and the microphone measurements at $\chi = 90$ deg. to characterize the fine scale turbulence noise component. The first row of data is measured in the minor axis plane. The second row is measured in a plane at 58 degrees to the minor axis plane. The third row is measured in the major axis plane. The last row is the data from a circular jet at the same jet velocity and total temperature. Within experimental uncertainty, it is clear from the table that the noise from the elliptic jet is, first of all, quite axisymmetric. Further, it is nearly the same as the circular jet. Table 2 provides direct comparisons between the $SPL_{\max}$ of the rectangular jet and a circular jet. Again, within experimental uncertainty, there is very little difference in the noise levels.

Tables 3 and 4 show the $SPL_{\max}$ data at $\chi = 150$ and 90 deg. for the various nozzles of the Yamamoto *et al.* experiments. It is worthwhile to remind the readers that the data are converted from $\frac{1}{3}$ octave band measurements and possibly slightly contaminated by shock and facility noise. The experimental uncertainty could be as large as 2 to 3 dB by our estimate. By comparing all the data with those of the C-D nozzle, it is evident that the differences are well within the experimental uncertainty. Thus, in spite of the large differences in nozzle geometry, the noise from supersonic jets

are remarkably the same. Based on these results, it is possible to surmise that nozzle exit geometry may not have significant control over the noise of high-speed jets.

4. CONCLUSION

Extensive comparisons between the noise radiated by supersonic jets operating at various temperatures and velocities with and without simulated forward flight and the noise from a circular jet at the same conditions have been carried out. Seven nozzles of practical geometries are included in the study. It is found that regardless of nozzle geometry, turbulent mixing noise of all the jets is comprised of two components. One component is the noise from the large turbulence structures and the other is noise from the fine scale turbulence of the jet flow. Further, the radiated sound is largely axisymmetric and that the shapes of the spectra of the two noise components are nearly the same as those of the similarity spectra of Tam, Golebiowski and Seiner[2]. In addition, the noise levels are essentially independent of nozzle configuration. Based on these results, it is concluded (bearing in mind the limited scope of this study) that nozzle geometry modification may not be an effective method for jet noise suppression.

ACKNOWLEDGMENT

This work was supported by NASA Langley Research Center Grant NAG 1-1776. The author wishes to thank Dr. J.M. Seiner for providing the elliptic and rectangular jet noise data. The valuable assistance of Nikolai Pastuchenko is hereby acknowledged.

Table 1. Elliptic jet (aspect ratio 3, $M_j = 1.98$)

	$\chi = 90$ deg.				$\chi = 141$ deg.				
T_r/T_∞	1.00	1.37	1.80	2.27	1.00	1.37	1.80	2.27	measurement plane
$SPL_{\max}$	74.3	75.5	77.0		96.8	99.5	101.7		minor axis plane
at $r = 100D_j$	74.3	75.7	76.8	78.3	96.1	98.8	100.3	101.3	58 deg. plane
(dB/Hz)	74.5	75.5	77.0	78.6	94.4	97.5	101.7	101.7	major axis plane
	75.5	76.2	77.3	78.5	97.3	99.3	100.7	102.1	circular jet

Table 2. Rectangular jet (aspect ratio 7.6, $M_j = 2.0$)

	$\chi = 90$ deg.			$\chi = 150$ deg.			
T_r/T_∞	1.10	1.82	2.26	1.10	1.82	2.26	measurement plane
$SPL_{\max}$	74.9	76.9	77.5	98.5	102.1	102.4	minor axis plane
at $r = 100D_j$	74.9	75.9	77.0	98.1	100.2	100.6	major axis plane
(dB/Hz)	76.0	77.7	78.8	98.4	101.5	102.6	circular jet

Table 3. Yamamoto *et al.* data
($v_j \simeq 2420$ ft/sec, $T_r \simeq 1715$ deg. R)

nozzle type	conical nozzle	C-D nozzle $M_d = 1.4$	convergent plug nozzle	C-D plug nozzle	suppressor nozzle	inlet angle χ, degree
$SPL_{\max}$ at	98.8	97.7	98.7	99.0	97.4	150
$r = 100D_j$ (dB/Hz)	77.6	75.0	76.6	77.2	74.5	90

Table 4. Yamamoto *et al.* data
($v_j \simeq 1720$ ft/sec, $T_r \simeq 870$ deg. R)

nozzle type	C-D nozzle $M_d = 1.4$	convergent plug nozzle	C-D plug nozzle	suppressor nozzle	inlet angle χ, degree
$SPL_{\max}$ at	95.0	96.2	97.1	92.5	150
$r = 100D_j$ (dB/Hz)	70.3	73.0	74.0	70.0	90

REFERENCES

[1] Westley, R. and Lilley, G.M., "An Investigation of the Noise Field from a Small Jet and Methods for Its Reduction," Report No. 53, College of Aeronautics, Cranfield (England), Jan. 1952.

[2] Tam, C.K.W., Golebiowski, M. and Seiner, J.M., "On the Two Components of Turbulent Mixing Noise from Supersonic Jets," AIAA Paper 96–1716, May 1996.

[3] Tam, C.K.W. and Chen, P., "Turbulent Mixing Noise from Supersonic Jets," AIAA Journal, vol. 32, Sept. 1994, pp. 1774–1780.

[4] Seiner, J.M., Ponton, M.K., Jansen, B.J. and Lagen, N.T., "The Effects of Temperature on Supersonic Jet Noise Emission," AIAA Paper 92–2046, May 1992.

[5] Tam, C.K.W. and Chen, K.C., "A Statistical Model of Turbulence in Two-Dimensional Mixing Layers," Journal Fluid Mechanics, vol. 92, part 2 1979, pp. 303–326.

[6] Yamamoto, K., Brausch, J.F., Janardan, B.A., Hoerst, D.J., Price, A.O., and Knott, P.R., "Experimental Investigation of Shock-Cell Noise Reduction for Single-Stream Nozzles in Simulated Flight," Comprehensive Data Report. Volume I. Test Nozzles and Acoustic Data, NACA CR–168234, May, 1984.

[7] Tam, C.K.W., "Supersonic Jet Noise," Annual Review Fluid Mechanics, vol. 27, 1995, pp. 17–43.

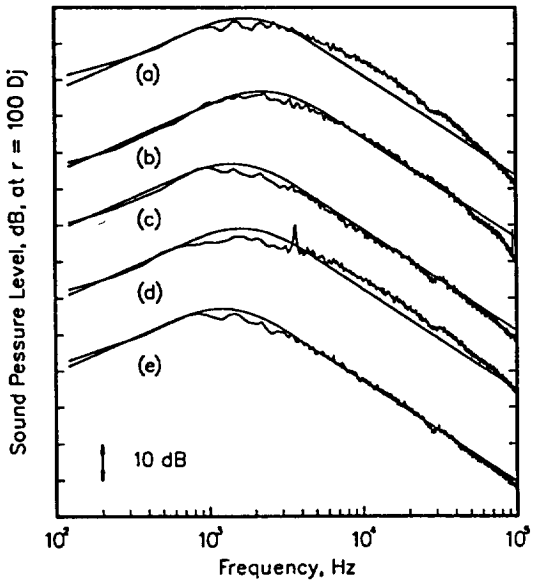

Figure 1. Comparisons between elliptic and rectangular jet noise data and the similarity spectrum at $\chi = 150$ deg., $\frac{T_r}{T_\infty} = 1.8$

Aspect ratio 3 elliptic jet: (a) minor axis plane, (b) 58 degree plane, (c) major axis plane.

Aspect ratio 7.6 rectangular jet: (d) minor, (e) major axis plane.

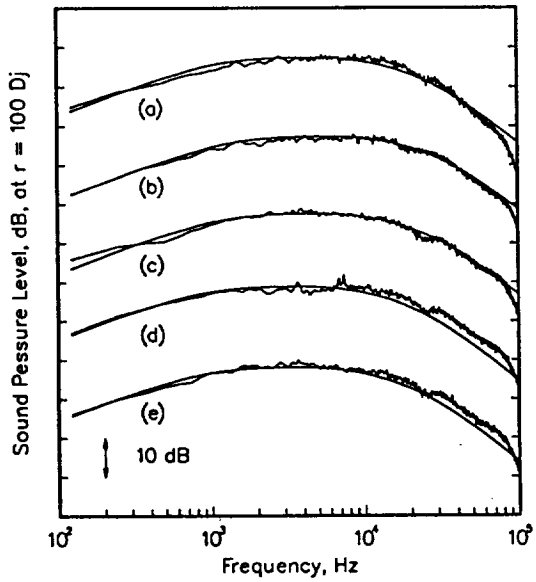

Figure 2. Comparisons between elliptic and rectangular jet noise data and the similarity spectrum at $\chi = 90$deg., $\frac{T_r}{T_\infty} = 1.8$

Aspect ratio 3 elliptic jet: (a) minor axis plane, (b) 58 degree pla ne, (c) major axis plane.

Aspect ratio 7.6 rectangular jet: (d) minor, (e) major axis plane.

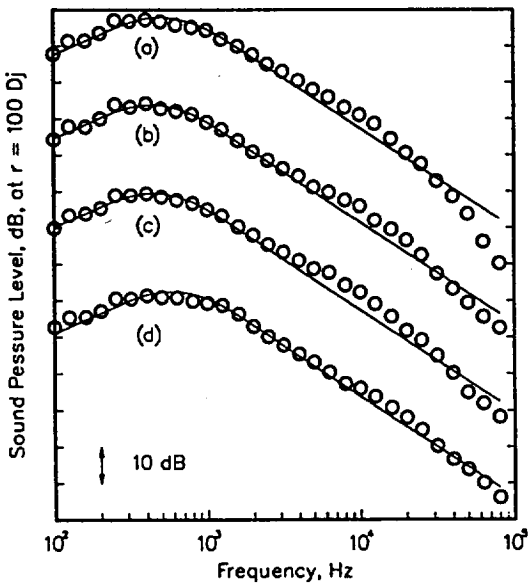

Figure 3. Comparisons between Yamamoto *et al.* data and the similarity spectrum. $V_j \simeq 2420$ ft/sec, $T_r \simeq 1715$ deg R, $\chi = 150$ deg; o data, ——— similarity spectrum. (a) C-D nozzle, (b) convergent plug nozzle, (c) C-D plug nozzle, (d) 20-chute C-D suppressor nozzle.

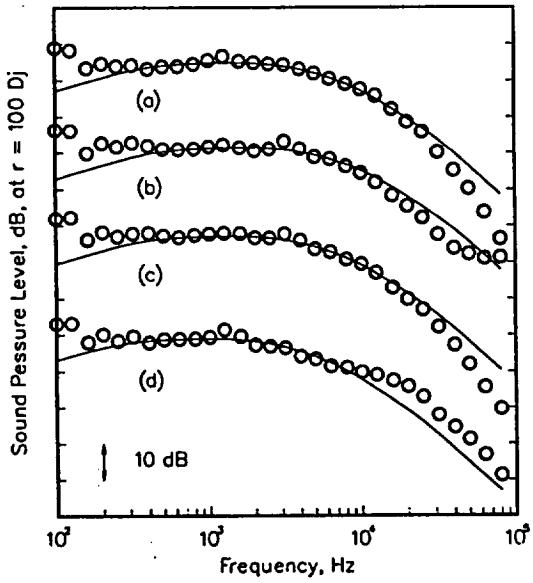

Figure 4. Comparisons between Yamamoto *et al.* data and the similarity spectrum. $V_j \simeq 2420$ ft/sec, $T_r \simeq 1715$ deg R, $\chi = 90$ deg; o data, ——— similarity spectrum. (a) C-D nozzle, (b) conve rgent plug nozzle, (c) C-D plug nozzle, (d) 20-chute C-D suppressor nozzle.